Mechanics-driven mechanobiological mechanisms of arterial tortuosity

Dar Weiss, Cristina Cavinato, Authia Gray, Abhay Ramachandra, Stéphane Avril, Jay Humphrey, Marcos Latorre

DISEASES AND DISORDERS

Mechanics-driven mechanobiological mechanisms of arterial tortuosity

Dar Weiss[1], Cristina Cavinato[1], Authia Gray[1], Abhay B. Ramachandra[1], Stephane Avril[2], Jay D. Humphrey[1]*, Marcos Latorre[1]

Arterial tortuosity manifests in many conditions, including hypertension, genetic mutations predisposing to thoracic aortopathy, and vascular aging. Despite evidence that tortuosity disrupts efficient blood flow and that it may be an important clinical biomarker, underlying mechanisms remain poorly understood but are widely appreciated to be largely biomechanical. Many previous studies suggested that tortuosity may arise via an elastic structural buckling instability, but the novel experimental-computational approach used here suggests that tortuosity arises from mechanosensitive, cell-mediated responses to local aberrations in the microstructural integrity of the arterial wall. In particular, computations informed by multimodality imaging show that aberrations in elastic fiber integrity, collagen alignment, and collagen turnover can lead to a progressive loss of structural stability that entrenches during the development of tortuosity. Interpreted in this way, microstructural defects or irregularities of the arterial wall initiate the condition and hypertension is a confounding factor.

INTRODUCTION

Notwithstanding the highly branched morphology of the vascular tree, most arterial segments are locally circular and relatively straight under normal conditions. This uniform geometry engenders locally uniform blood flow that is efficient for fluid transport as well as uniform states of flow-induced wall shear stress and pressure-induced intramural stress consistent with local mechanical homeostasis (*1*). Since at least the time of Leonardo da Vinci (1452–1519), however, it has been known that different conditions give rise to persistent abnormal bends, twists, turns, and kinks within arteries that are generally referred to as tortuosity. Advances in modern medical imaging, genetics, and clinical phenotyping continue to reveal more and more conditions that either cause or are a consequence of arterial tortuosity. In addition to arterial tortuosity syndrome, which disrupts a glucose transporter and compromises elastic fibers within the arterial media (*2*), vascular aging and hypertension and similarly genetic conditions that predispose to thoracic aortopathies also associate with arterial tortuosity (*3*–*6*). Given the underlying mechanical basis of circulatory physiology and vessel mechanobiology, it is not unexpected that arterial tortuosity has been associated with altered mechanical factors, including changes in blood flow and pressure, axial tension, and the structural composition of the arterial wall (*7*, *8*). Nevertheless, the biomechanical mechanisms responsible for the development of tortuosity have remained unclear.

Here, we combine a custom digital imaging correlation method with optical coherence tomography (OCT) to study in greater detail the local mechanics of native and tortuous thoracic aorta in a well-accepted genetically modified mouse model of compromised elastic fiber integrity. We then use an experimentally informed mechanobiologically motivated computational model of aortic growth and remodeling (G&R) to test competing hypotheses on the underlying mechanisms by which these vessels become tortuous. Although most previous attention has been directed toward the possibility of an elastic structural buckling instability (*7*, *9*), it has been acknowledged that such an intermittent response does not describe the marked, persistent tortuosity observed in vivo but rather leads to modest deflections under physiological pressures (*10*, *11*). Our experimental-computational findings suggest that arterial tortuosity likely arises via progressive cell-mediated responses to local imperfections and aberrant microstructural changes that can develop within an aged or diseased arterial wall, with reduced axial tension and elevated blood pressure exacerbating these maladaptive responses. The importance of understanding the underlying mechanical and mechanobiological mechanisms of arterial tortuosity is underscored by both the need to understand better the clinical time course and especially the desire to use tortuosity as a reliable biomarker for diverse vascular conditions (*6*, *8*).

RESULTS

Absence of fibulin-5 reduces aortic distensibility and increases tortuosity

Relative to the descending thoracic aorta in age- and sex-matched wild-type mice, aorta from *Fbln5*$^{-/-}$ mice exhibit a lower structural distensibility (i.e., normalized changes in diameter per changes in pressure) despite modest reductions in biaxial material stiffness (table S1). They also develop considerable tortuosity in vivo (fig. S1), which persists in situ in the absence of pressurization and in vitro whether pressurized or not (Fig. 1, A and B, and fig. S2). Reconstructions of the three-dimensional (3D) geometry of the aorta in vitro (Fig. 1C) reveal further that the degree of tortuosity increases transiently with increases in distending pressure (Fig. 1D), which, as expected, is significantly greater in *Fbln5*$^{-/-}$ mice compared with wild type ($P < 0.001$ for mixed comparisons between 52- and 20-week-old groups). Quantification of bulk mechanical properties revealed few overall differences between the two *Fbln5*$^{-/-}$ age groups or between the two wild-type groups: Distributions of circumferential and axial material stiffness were not significantly different across the four groups (Fig. 1, E, F, H, and I), although the absence of fibulin-5 reduced elastic energy storage capability relative to control ($P < 0.01$ between *Fbln5*$^{+/+}$ and *Fbln5*$^{-/-}$ groups;

[1]Department of Biomedical Engineering, Yale University, New Haven, CT, USA. [2]Mines Saint-Etienne, Centre CIS, INSERM, U 1059 Sainbiose University of Lyon, Univ Jean Monnet, Saint-Etienne, France.
*Corresponding author. Email: jay.humphrey@yale.edu

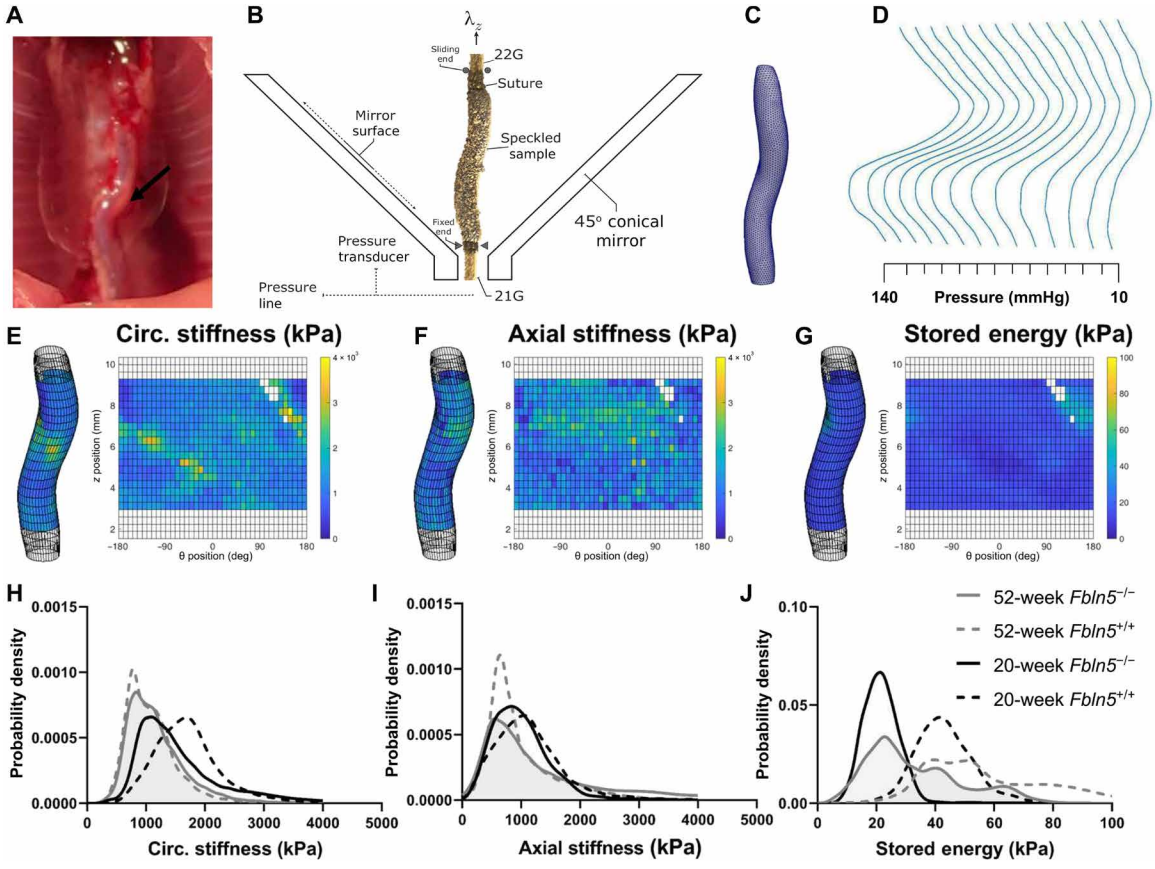

Fig. 1. pDIC data collection and analysis. (**A**) Representative in situ image (photo credit: Dar Weiss, Yale University) of a tortuous descending thoracic aorta at zero blood pressure (arrow) in a 20-week-old *Fbln5*$^{-/-}$ mouse, which was excised and (**B**) mounted on a custom triple-needle assembly for placement in the panoramic digital image correlation (pDIC) system (fig. S2). Centerlines were computed for each (**C**) 3D reconstructed configuration at the sample-specific in vivo axial stretch and (**D**) used to calculate a tortuosity index (TI) at each pressure applied in vitro. Using the virtual field-based inverse method, spatial distributions of (**E**) circumferential and (**F**) axial material stiffness, (**G**) elastic stored energy, and other metrics (fig. S3) were identified and superimposed on the reconstructed reference configuration geometry (at in vivo axial stretch and 80 mmHg) and then unwrapped and plotted in $\theta - Z$ planes around the vessel circumference ($\theta \in [-180,180]$) and along its (Z) axial extent. The rightmost edge of each 3D rendering is at about 0°, whereas the leftmost edge is at about ±180°; see the middle panel of Fig. 3 for further clarification of the mapping from 3D to 2D. Edges of the samples and patches with a poor coefficient of determination were neglected and left blank. Averaged probability density functions are shown in the third row, comparing the entire distributions of (**H**) circumferential and (**I**) axial stiffness as well as (**J**) stored energy over the four study groups.

Fig. 1, G and J), which was exacerbated slightly (not significantly) by aging from 20 to 52 weeks.

Tortuosity correlates with reduced distensibility and deformability

Aortic tortuosity in *Fbln5*$^{-/-}$ aortas correlates well with decreasing structural distensibility and biaxial deformability (Fig. 2), that is, reduced values of circumferential and especially axial stretch upon mechanical loading. As seen in the figure, the degree of tortuosity also correlates with reduced energy storage capability (reflecting compromised elastic fiber integrity), the key metric that is significantly different between wild-type and fibulin-5–null aortas. Whereas energy storage reflects a fundamental mechanical functionality of the wall (i.e., the normal aorta stores elastic energy during systole and uses this energy during diastole to work on the blood to augment flow), circumferential material stiffness appears to be highly mechanoregulated within the arterial wall (*12*). There was little correlation between tortuosity and either circumferential or axial material stiffness (fig. S4), suggesting that the intramural cells were yet able to sense and regulate the stiffness of the matrix on average.

Multimodality imaging reveals regional differences in structure and properties in tortuosity

Figure 3 contrasts calculated values of circumferential and axial stretch and similarly biaxial material stiffness within concave and convex regions of the tortuous aorta in *Fbln5*$^{-/-}$ mice. Notwithstanding considerable variations, circumferential material stiffness was significantly higher and circumferential stretch was significantly lower on the convex compared with the concave sides of the tortuous aorta. Axial stretch tended to be significantly greater on the convex side, although axial stiffness differed little between the two sides. In addition, the proximal-convex region exhibited significantly higher systolic-to-diastolic differences in elastically stored energy compared with the proximal-concave region, while differences in the distal region were negligible (fig. S5).

Multiphoton microscopy—both second-harmonic generation revealing fibrillar collagen and autofluorescence revealing elastin-based structures—provided complementary information on local microstructure. The medial layer appeared nonuniform and scattered in the *Fbln5*$^{-/-}$ aorta due to agglomerations containing irregular-shaped elastin (Fig. 4A), not compact lamellar structures,

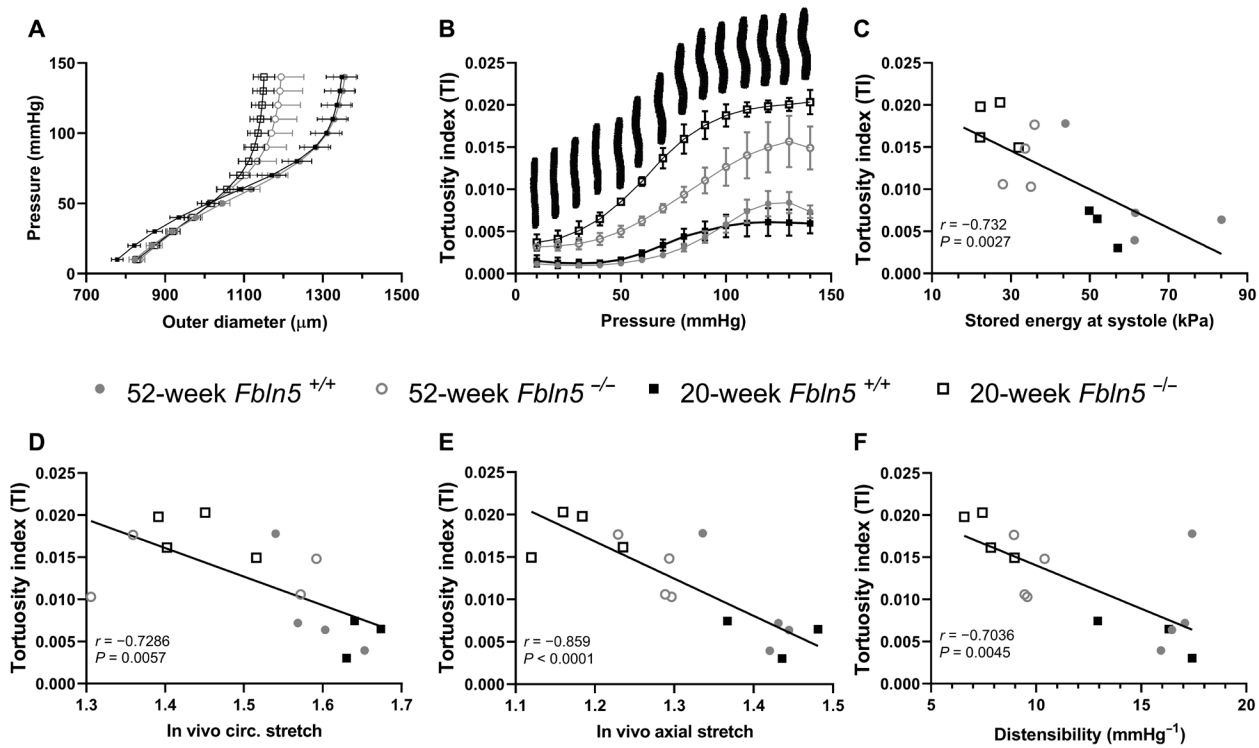

Fig. 2. Tortuosity correlates with reduced distensibility and deformability. (**A**) In vitro pressure versus loaded outer diameter curves for the four study groups reveal structural stiffening in the *Fbln5*$^{-/-}$ groups. (**B**) A TI was calculated at each pressure (10 to 140 mmHg) at the specimen-specific in vivo axial stretch. Data are shown as means ± SEM for each group. Note the marked differences in TI between *Fbln5*$^{+/+}$ and *Fbln5*$^{-/-}$ aortas, with pressure-dependent changes in geometry exemplified above one TI versus pressure curve. The in vitro measured TI was plotted against the (**C**) stored energy and (**D**) circumferential stretch at 120 mmHg and against the (**E**) in vivo axial stretch and (**F**) structural distensibility, defined as $(d_2 - d_1)/d_1(P_2 - P_1)$, where d denotes diameter and P denotes pressure, with $P_2 > P_1$. Each point represents the mean of the distribution of one sample. Note the significant ($P < 0.05$) negative correlation between TI and all four metrics. Correlations were evaluated using the Pearson correlation coefficient, r.

or well-organized elastic fiber networks as in normal vessels; there were, however, no apparent differences in smooth muscle cell density between the concave and convex regions (fig. S5). Overall wall thickness was lower in convex compared with concave regions of the tortuous *Fbln5*$^{-/-}$ aorta (Fig. 4B), with loaded thickness significantly less in 52- than 20-week-old samples (fig. S5). Yet, the convex regions had a significantly ($P < 0.05$) thicker adventitia than did the concave regions, with adventitial fraction not different in 20- and 52-week-old *Fbln5*$^{-/-}$ samples.

The adventitial layer in the tortuous *Fbln5*$^{-/-}$ aortas consists of multiple layers of fibrillar collagen bundles inclined toward a primary orientation that corresponds, at the in vivo axial stretch and physiological distending pressures, with the overall axial direction of the vessel (Fig. 4A), consistent with previous observations (*13*). Although this primary orientation did not differ significantly, upon pressurization, between the convex and concave regions or between the 20- and 52-week *Fbln5*$^{-/-}$ mice, the degree of dispersion of fiber orientation around the primary direction did vary (Fig. 4C), with collagen fibers dispersed significantly more in convex compared to concave regions in the 20-week-old *Fbln5*$^{-/-}$ samples, while this characteristic was inverted in 52-week-old *Fbln5*$^{-/-}$ samples, with a higher dispersion of the fibers in concave regions. The orientation dispersion increased with pressure in most regions, indicating load-induced reorientation from axial toward symmetrically diagonal directions to counter the increasing pressure, as expected. The only case that showed an opposite trend, on average, was the convex region of 52-week *Fbln5*$^{-/-}$ samples.

Computational modeling reveals mechanisms of tortuosity

Data-informed computational simulations enable numerical examinations of competing hypotheses. Simulations confirmed that the normal aorta is robust against modest local perturbations in material properties, geometry, and perivascular support (Fig. 5), consistent with the general absence of tortuosity in the wild-type aorta (figs. S1 and S3). Specifically, the central column of Fig. 5 shows fully resolved adaptations of an initially straight cylindrical segment of a normal aorta having uniform geometry and material properties and subjected to in vivo homeostatic conditions of blood pressure, flow, and axial stretch plus local perturbations (two sites reflecting those observed in a representative *Fbln5*$^{-/-}$ sample) in material properties (modest local changes in elastin and collagen parameters; top row), perivascular tethering (mild local "push" and "pull"; middle row), or local geometry (slight overall undulations superimposed on the straight segment; bottom row).

In stark contrast, allowing wild-type material properties to degenerate toward those of the fibulin-5–null aorta (namely, uniformly decreasing the parameter governing elastic fiber contributions to overall wall stiffness and evolving the parameter governing the orientation of diagonal families of collagen fibers to reflect an increased circumferential orientation; table S2) rendered the vessel vulnerable

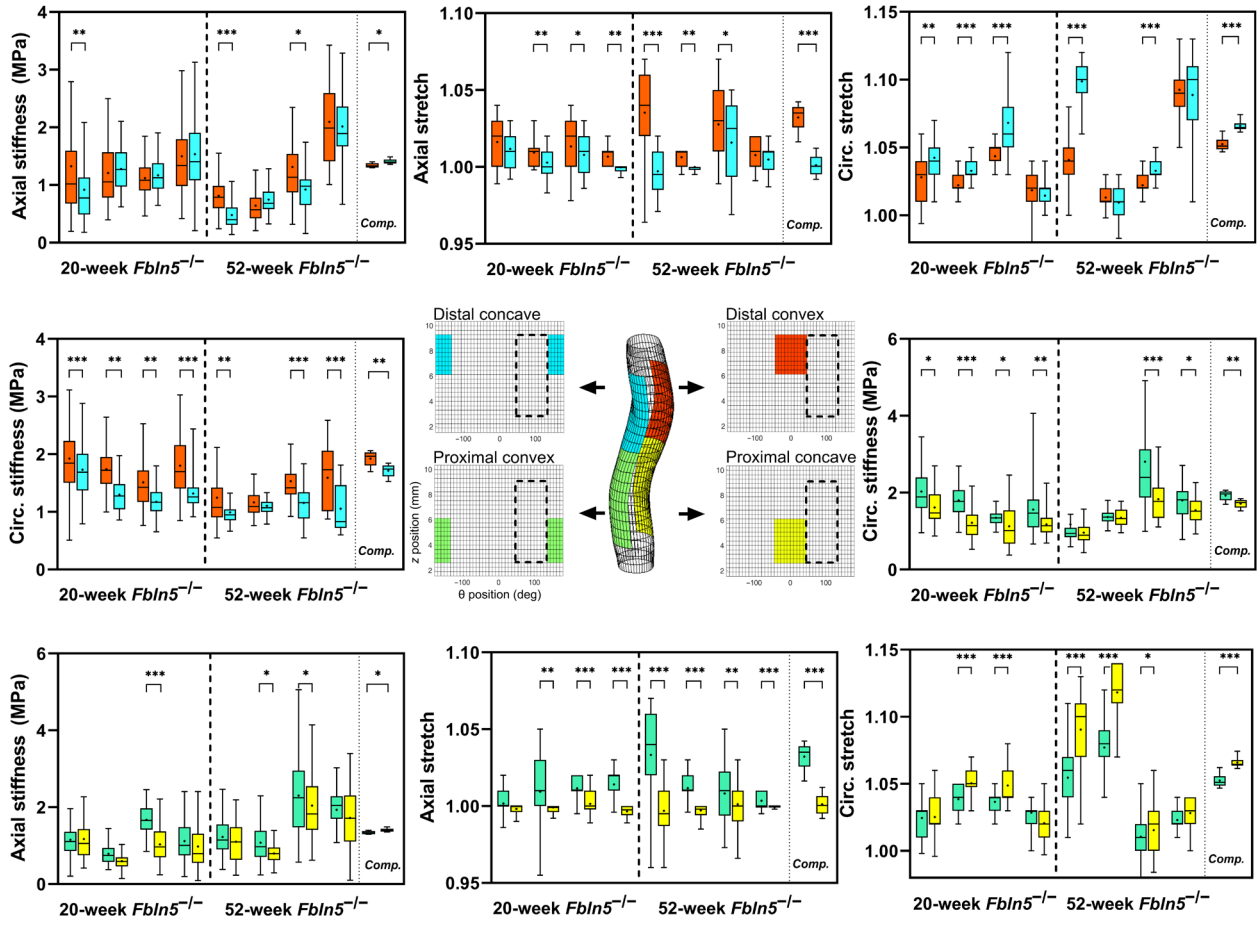

Fig. 3. pDIC reveals regional differences in structure and properties in tortuosity. Inflection points, defined on the aortic centerline (Fig. 1), were used to divide all *Fbln5*$^{-/-}$ samples into four local regions along the long axis of the vessel: proximal (green and yellow), distal (blue and orange), convex (green and orange), and concave (yellow and blue), each consisting of ~100 elements. Box plots (average denoted by *) compare biaxial material stiffness and stretch at 120 mmHg between convex and concave regions at proximal and distal ends. Note the markedly higher circumferential (Circ.) stiffness and axial stretch and lower circumferential stretch in convex regions. The far-right column within each panel (separated by a dotted line and denoted Comp.) shows results from the computational G&R simulations (see below), confirming the same trends between convex and concave regions. The computational results for the proximal and distal ends are identical and are shown on all panels for clarity. An overbar denotes statistical significance between regions, with $^{*}P < 0.05$, $^{**}P < 0.01$, and $^{***}P < 0.001$. Effect sizes are shown in table S3. Last, note that the intercostal branches are anatomically outside of the four selected regions (black dashed rectangles in the center panel) and were excluded from data analysis. Consistent with Fig. 1, the rightmost edge of each 3D rendering is at about 0°, whereas the leftmost edge is at about ±180°; see the middle panel for further clarification of the mapping from 3D to 2D.

to local perturbations under isometric, but not isotonic, end conditions (Fig. 5). Specifically, degeneration of wild-type properties tended to relax the in vivo axial stress and induce an axial G&R response despite the constant blood pressure and flow. Enforcing a constant axial tension at the ends (isotonic boundary condition, left column in Fig. 5) could progressively restore the level of axial stress, hence enabling a nearly straight elongation in vivo and preventing the development of a tortuous vessel. Conversely, enforcing a constant end-to-end length (isometric boundary condition; right column) inevitably allowed the axial unloading to progress via extracellular matrix turnover in evolving states, with an increasingly lower axial tension and an increasingly higher lateral force contributing to out-of-plane deformations and development of tortuosity.

Note, too, that the far-right column in each of the panels in Fig. 3 compares mean results from one of these G&R simulations (top right in Fig. 5, for which higher regional differences were observed, consistent with differential growth induced by the nonuniform local perturbation in material properties) against the measured regional results for biaxial stretch and material stiffness from the experiments on the fibulin-5–null aorta, thus confirming the goodness of the in silico simulations and, in particular, that mechanobiologically stimulated turnover of extracellular matrix in evolving mechanical states can lead to a progressive, persistent tortuosity.

Figure 6 highlights one particular progression of tortuosity (absent-to-severe) for the case of initially perturbed elastin and collagen properties, with regional values of biaxial wall stress and material stiffness shown superimposed on the tortuous vessel. The local change in wall volume (or mass given constant tissue density) is also shown (bottom row), consistent with the simulated (i.e., emergent, not prescribed) G&R response to the imposed insults. Such simulations can be stopped at any intermediate time and, with G&R frozen, isochoric elastic stress-strain responses can be computed for transient changes in blood pressure and/or axial extension, hence simulating a biaxial mechanical test. Figure S6 shows such a distension test performed

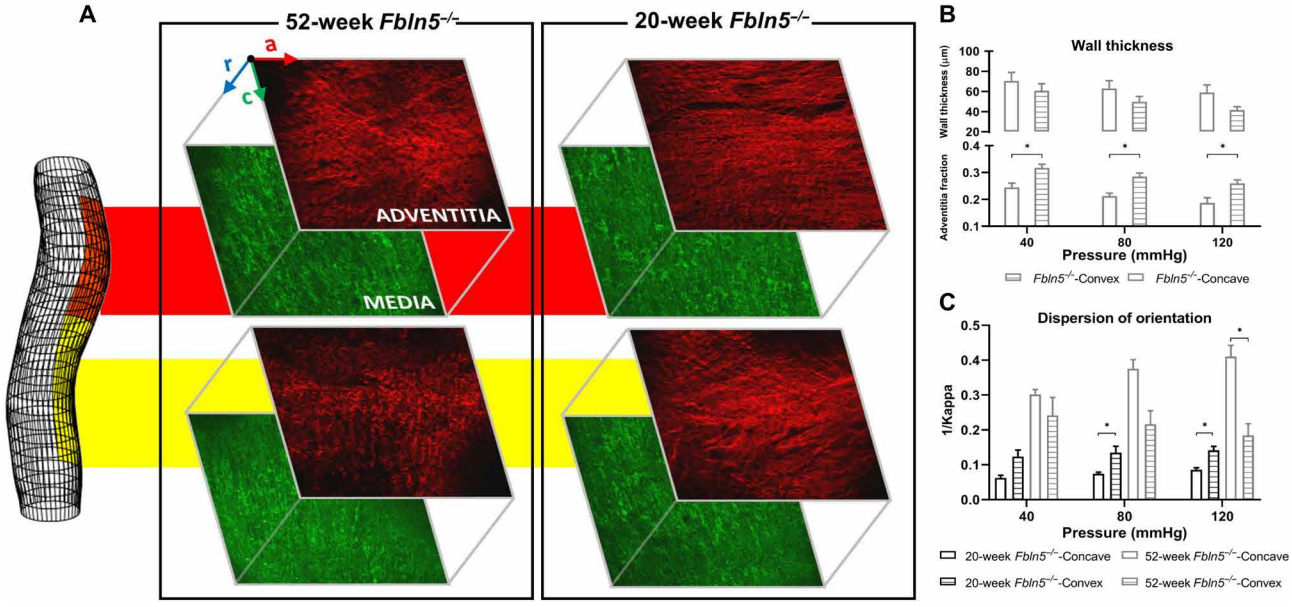

Fig. 4. Multiphoton microscopy. (**A**) 3D images for convex and concave regions of 20- and 52-week-old *Fbln5*$^{-/-}$ aortas, shown here for selected axial-circumferential slices at specimen-specific in vivo axial stretch and 80 mmHg. Collagen appeared as undulated bundles with a preferential orientation in the adventitia; elastin-based structures were irregular and scattered in all regions, as expected with the absence of fibulin-5. (**B**) Mean thickness of the wall and adventitia obtained from multiple 3D images (age groups merged) at three physiologic pressures and the sample-specific axial in vivo axial stretch (see fig. S5, age effects). Adventitial thicknesses were normalized by, and thus independent of, overall wall thickness, which was lower in convex than in concave regions, with a higher fraction of adventitia in convex compared to concave regions and, consequently, the opposite for the medial fraction. (**C**) Orientation dispersion of collagen fibers determined for concave and convex regions at three different physiologic pressures and the sample-specific axial in vivo stretch. Higher dispersion manifested in the convex region compared to the concave regions in 20-week *Fbln5*$^{-/-}$, while 52-week *Fbln5*$^{-/-}$ had higher dispersion in concave regions. Aging increased the fiber orientation dispersion. Significance denoted by $*P < 0.05$.

on the partially tortuous artery seen in Fig. 6 (second from the right column) at the in vivo value of axial stretch (central column, in vivo systolic pressure). Although the degree of tortuosity is greater at higher pressures (right column) and less at lower pressures (left column), marked changes in pressure (from 80 to 160 mmHg) induce only moderate elastic bends when computed on an otherwise vulnerable vessel. The local invariance in wall volume (or mass) during transient loading is also shown (bottom row), consistent with the simulated isochoric elastic response with locally preserved (i.e., from the previous frozen simulation) material insults.

To explore further the effect of the initial degree of tortuosity on the subsequent elastic bending response (see Fig. 1D), the first row in fig. S7 shows how a distension test performed on the same vessel at a time when the degree of growth-induced tortuosity is lower (Fig. 6, second from the left column) generates a much lower effect on the tortuosity. In stark contrast, fig. S7 (second row) shows that this modest axial growth–induced tortuous remodeling increases notably when a moderate increase in systolic pressure up to $P = 135$ mmHg (<160 mmHg for the elastic distension test) is combined with the underlying partial change in material properties from normal, hence reinforcing the idea that tortuosity develops from a progressive mechanobiological, not just mechanical, structural instability. The (initially perturbed) normal aorta did not remodel into a tortuous geometry when subjected to the same increases in pressure, suggesting that persistent hypertension is a risk factor only for previously compromised vessels.

Last, fig. S7 (last row) shows how, once tortuosity has developed (see Fig. 5, top left), a responsive change in the maximal regional orientation of diagonal fibers from the convex toward the concave regions (left to right, simulating the inverted trend for the dispersion of collagen fibers observed for 52-week-old *Fbln5*$^{-/-}$ samples relative to 20-week-old *Fbln5*$^{-/-}$ samples; see Fig. 4C) cannot resolve the permanent tortuosity of this compromised, yet axially unloaded, computational aorta. This last finding suggests that arteries that have grown and remodeled into a marked tortuous pattern may be mechanobiologically and structurally stable against possible reverse remodeling, even if new spatial nonuniformities are inverted with respect to the (otherwise critical) perturbations that contributed to dictate the developing arterial shape.

DISCUSSION

It is well known that in vitro and ex vivo distension tests on isolated cylindrical segments of even a normal artery can provoke a reproducible, reversible pressure-induced bending that depends on the length of the specimen, the degree of its fixed axial pre-stretch, and the magnitude of the pressure applied. Critical distending pressures that induce such bending are reduced at lower values of axial extension, and this phenomenon can be understood as an elastic buckling instability (*7*). Given the clinical associations of tortuosity with conditions of compromised elastic fiber integrity—aging, arterial tortuosity syndrome, Loeys-Dietz syndrome, Marfan syndrome, and so forth—considerable attention to understanding such buckling in vitro has appropriately focused on experimental models of defective, damaged, or degraded elastic fibers. Years ago, Dobrin *et al.* (*14*) treated excised canine carotid arteries with elastase and suggested that loss of elastin releases axial stress within an artery held at a fixed length, thus increasing its potential to buckle. Lee *et al.* (*15*) confirmed that

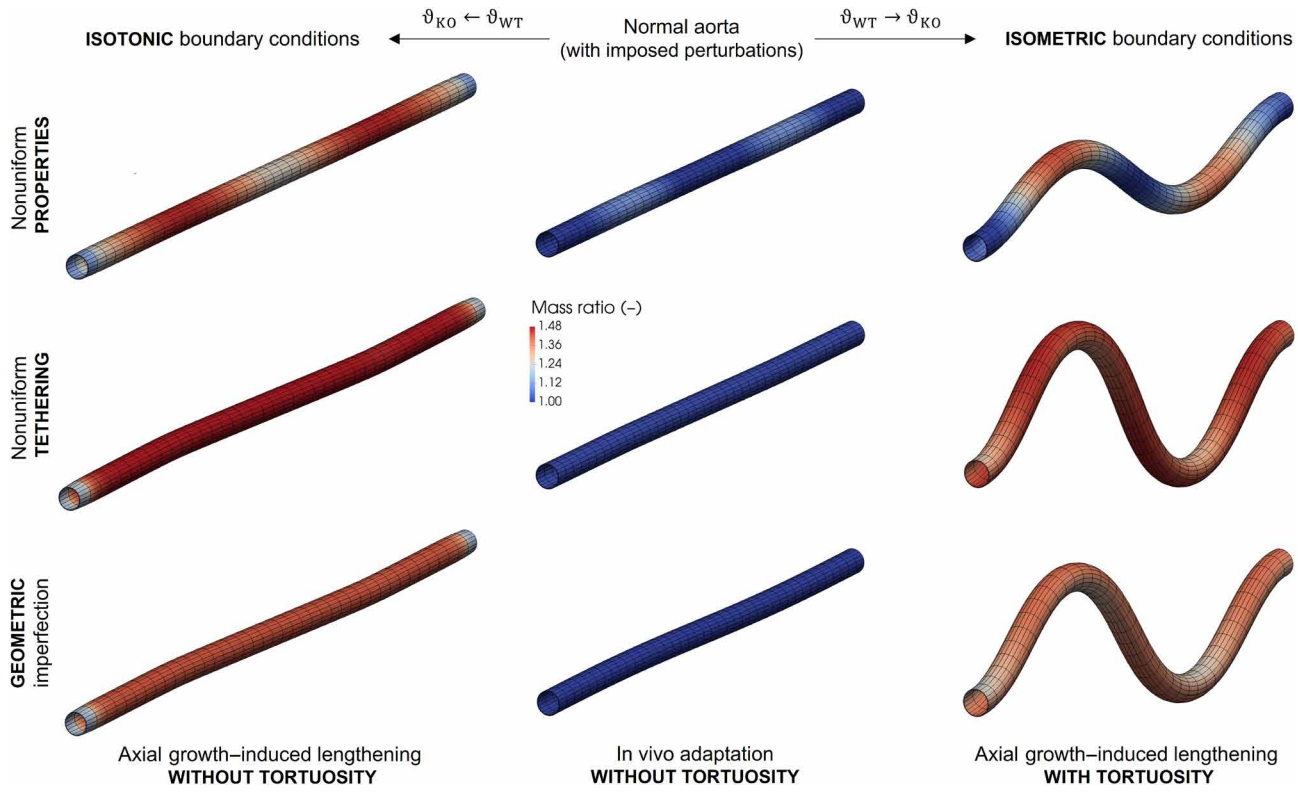

Fig. 5. Computational modeling reveals mechanisms of arterial tortuosity. Fully resolved, mechano-adapted, G&R responses (central column)—predicted for an initially straight cylindrical aortic segment having normal uniform geometric and material properties ($\vartheta = \vartheta_{WT}$) subjected to in vivo homeostatic conditions of blood pressure, flow rate, and axial stretch (representing an idealized *Fbln5*$^{+/+}$ sample, not shown)—to local insults (two sites reflecting that observed via pDIC in a representative *Fbln5*$^{-/-}$ sample) in material properties (representing a modest local loss of elastic fiber integrity and remodeling of diagonal families of collagen toward the circumferential direction, top row), a change in perivascular tethering (mild local push and pull, middle row), or a change in local geometry (prescribed slight overall undulations, bottom row). Next, for all three types of insults considered here, a marked degeneration in elastin and collagen parameters toward those of the fibulin-5–null aorta ($\vartheta_{WT} \rightarrow \vartheta_{KO}$) induces a severe axial growth response under in vivo blood pressure and flow, which leads to a nearly straight lengthening of the aorta for a constant axial tension prescribed at the ends (isotonic boundary condition, left column) but a markedly tortuous elongation for fixed ends (isometric boundary condition, right column). See Materials and Methods for definitions of ϑ.

critical buckling pressures are lower in vitro for elastase-treated than native porcine carotid arteries, while Luetkemeyer *et al.* (*11*) reported similar findings for elastin haploinsufficient (*Eln*$^{+/-}$) murine carotid arteries. Conversely, increased smooth muscle cell tone can increase the critical buckling pressure (*16*), whereas perivascular support can change the buckling mode (*15*). Although these studies provide valuable insight, there is no clear evidence that such instantaneous (elastic) buckling occurs in vivo; moreover, such buckling resolves instantaneously when pressure is lowered, and it has been suggested that this type of buckling alone cannot explain the marked, persistent tortuosity observed in patients or mouse models. Even investigators focusing on elastic buckling instabilities suggest that one should consider arterial G&R as fundamental to the process of tortuosity (*10*, *11*, *17*).

On the basis of clinical observations, many speculate that tortuosity develops from the axial growth of an artery in the presence of geometric constraints, including branches or sites of attachment to perivascular structures (*6*, *18*). Langille and colleagues (*18*, *19*) showed directly in an in vivo rabbit model that surgically induced increases in axial loading of the carotid artery initiate a rapid cell-mediated G&R response that reduces the axial wall strain back to normal within 1 week while maintaining a straight geometry (captured by our model, see left column in Fig. 5), consistent with ex vivo findings (*20*) and the concept of mechanical homeostasis (*21*). In contrast, surgically induced decreases in axial loading result in marked persistent tortuosity and normal cell-mediated responses cannot resolve this tortuosity, at least over a period of weeks (see Fig. 5, right column). These experimental findings are consistent with clinical inference and early in vitro observations, suggesting that reducing axial tension within a vessel can lead to persistent tortuosity in vivo, although the mechanisms remained largely unknown.

The descending thoracic aorta is a common site of tortuosity, especially in aging (*22*), with a slight bias toward increased frequency in females (*23*). Rather than study sex as a biological variable, we focused on adult female mice aged 20 or 52 weeks. Moreover, rather than focusing on elastic buckling of pressurized arteries in vitro, we studied directly both normal and tortuous descending thoracic aortas using *Fbln5*$^{+/+}$ and *Fbln5*$^{-/-}$ mice from the same breeding colony, the latter of which have compromised elastic fiber integrity (*24*), exhibited marked tortuosity in vivo (*25*), and represented a model of arterial aging (*26*). We used a four-fiber family constitutive relation that has proven useful in describing the mechanics of murine arteries (*24*) and has been independently validated as the best of many common descriptors, even for describing buckling (*11*). Notwithstanding the high fidelity and general utility of biaxial extension-distension tests

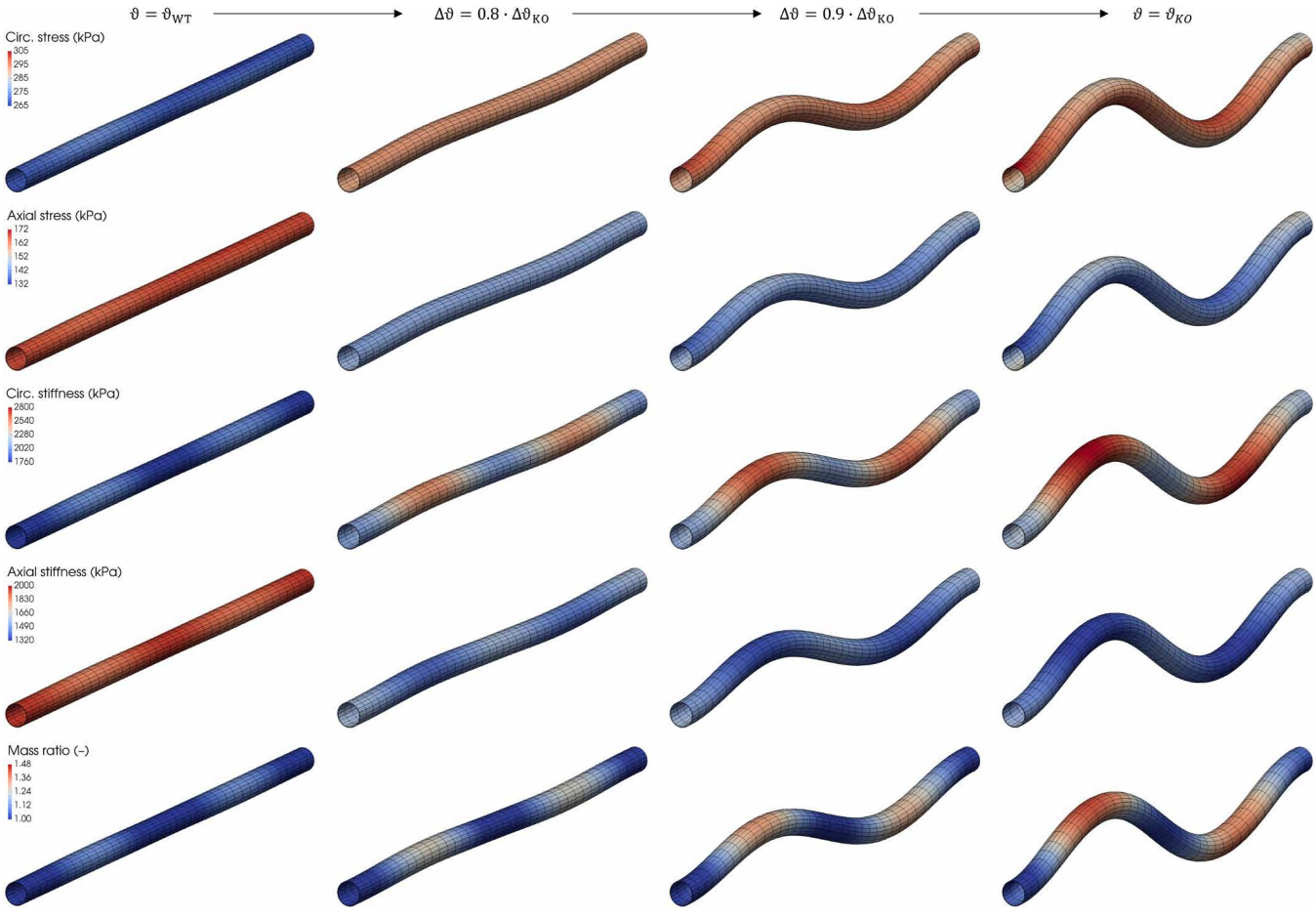

Fig. 6. Abnormal axial elaboration of tissue off-loads the vessel and gives rise to tortuosity. Progressive initiation and development of persistent tortuosity (i.e., remaining in the absence of loading) for a normal aortic segment (left column; $\vartheta = \vartheta_{WT}$, including a modest change in local properties at two sites) induced by an increasingly greater loss of elastic fiber integrity $\Delta\vartheta = \Delta c^e = c^e - c^e_{WT}$ combined with a gradual increase in orientation of diagonal fibers of collagen $\Delta\vartheta = \Delta\alpha_0 = \alpha_0 - \alpha_{0WT}$ (left to right) up to $\vartheta = \vartheta_{KO}$ (right column); see table S2. Shown superimposed on the tortuous vessel are the regional values of biaxial wall stress (first and second rows), material stiffness (third and four rows), and change in wall volume (fifth row), the last revealing a gradual increase in mass by deposition along the axial direction (with luminal radius and wall thickness nearly preserved throughout). The G&R model predicted both an initial axial off-loading (second row) of the nearly straight artery until the loss of its structural stability (pre-buckling response, $\Delta\vartheta \lesssim 0.8 \cdot \Delta\vartheta_{KO}$) and a tortuous remodeling that follows the instability (post-buckling response due to matrix turnover in evolving states, $\Delta\vartheta > 0.8 \cdot \Delta\vartheta_{KO}$), with a smooth transition between phases afforded by the initial local perturbation. See Materials and Methods for definitions of ϑ.

in characterizing bulk mechanical properties of the murine vasculature (Fig. 2), the uniqueness of our validated panoramic digital image correlation (pDIC) + OCT inverse approach to quantify local material properties (*27*) revealed marked regional variations in properties within the tortuous aorta that manifest at major bends (convex versus concave aspects) therein (Fig. 3).

Motivated by these experimental findings, we developed a constrained mixture finite element model of aortic G&R to numerically contrast multiple competing hypotheses. The general theoretical framework upon which this model rests has proven reliable in describing diverse vascular adaptations and maladaptations (*28*) and here predicted an emergent, progressive, persistent tortuosity similar to that observed experimentally. The model suggested that a uniform loss of elastic fiber integrity elicits a G&R response under homeostatic loading, but this alone does not lead to tortuosity. Rather, an additional change in material properties (realigned diagonal collagen fibers) is needed to stimulate a potent axial growth response and associated axial off-loading that, in combination with an imposed localized perturbation in properties, initial geometry, or perivascular tethering, induces progressive tortuosity if and only if aortic displacements are fixed at the ends. That is, tortuosity does not develop in an otherwise vulnerable vessel that is maintained under a constant axial tension (i.e., with axial strain continuously restored back to normal via G&R in evolving configurations), which simply elongates while maintaining a nearly straight geometry. Hence, the current simulations are consistent with experimental observations from in vitro and in vivo tests that loss of axial loading via longitudinal elaboration of new tissue contributes to the development of tortuosity (*19*), but suggest further that anatomical constraints and local structural imperfections or loading nonuniformities are critical in driving tortuosity when particular material properties differ from normal. Our findings regarding roles of an increased ratio of circumferential-to-axial stiffness and axial unloading (Fig. 6) are consistent with finite element simulations of tortuosity in veins (*29*), although that previous study called for, but did not include, the essential mechanobiologically driven G&R response that we included.

Others have considered G&R effects when performing linearized stability analyses of arteries. Goriely and Vandiver (*17*) showed beneficial roles of residual stresses (induced via previous growth) and axial stretch in preventing elastic buckling of arteries under internal pressure. Liu *et al.* (*30*) analyzed the mechanical stability of collateral arterioles and concluded that they become prone to buckling due to a combination of axial and radial growth. Notwithstanding the utility of these and similar studies to detect elastic bifurcations, which define critical loads and associated mode shapes under which a tortuous response may initiate, such linear (pre-buckling) stability analyses cannot describe the fully nonlinear (post-buckling) G&R response that may develop after the onset of an initial instability. Furthermore, growth was previously prescribed without connection to the evolving stress or strain fields, although it is well known that G&R responses are inherently coupled with the mechanics through the mechanosensitive responses of the cells of the arterial wall (*1*).

By contrast, we used a fully nonlinear (geometrically and materially), mechano-regulated, G&R computational model capable of describing both the initiation and subsequent development of tortuosity (with a smooth transition under in vivo conditions) based on multiple microstructural hits informed by our experimental study. It is worth noting that other fully nonlinear frameworks have been used to study growth-induced structural instabilities involving other soft tissues, as, for example, cortical folding in the developing brain (*31*, *32*), but not tortuosity in arteries, especially when accounting for the differential material properties of the different structural constituents that make up the arterial wall, which proved particularly critical in our constrained mixture model of G&R.

Many conditions that associate with arterial tortuosity clinically appear to suggest that a loss of elastic fiber integrity alone increases the possibility of tortuosity (*6*, *23*), consistent with in vitro studies showing that elastase treatment and genetic reductions in elastin synthesis decrease the critical pressure at which an elastic buckling instability manifests during in vitro distension tests (*11*, *14*, *15*). However, the in vitro determined critical buckling pressure of the carotid artery was lower in the $Eln^{+/-}$ mouse than in the $Fbln5^{-/-}$ mouse (*11*), yet there is no reported in vivo tortuosity in $Eln^{+/-}$ mice, which are hypertensive, compared with the $Fbln5^{-/-}$ mouse, which is normotensive. It is unclear, therefore, whether in vitro elastic buckling studies alone can predict in vivo tortuosity. By contrast, the present experimental-computational study suggests that compromised elastic fiber integrity represents a critical vulnerability but only when combined with an increased collagen-related circumferential-to-axial stiffening and axial unloading, fixed displacements at the ends of the vessel, and localized perturbations from normal, including material imperfections, nonuniform tethering, or an aberrant local curvature. Our model allowed each of these conditions to be prescribed conveniently and compared directly in sites reflecting those in the tortuous fibulin-5–null aortas; additional combinations of insults may further exacerbate the tortuosity.

Regardless, the numerically simulated distension tests revealed further that the extent of the associated elastically induced bending is proportional to the underlying, previously manifested, G&R-induced tortuosity. That is, our findings suggest that the normal aorta, even in the presence of kinematic constraints and structural imperfections, is yet robust against tortuosity and that multiple hits must coexist for vessels to grow and remodel into a persistent tortuous geometry. Of course, loss of elastic fiber integrity can alter smooth muscle cell proliferation (*33*), and altered axial loading can change the mitotic axis of the mural cells (*34*), hence emphasizing the importance of mural composition and loading on the mechanobiology, not just the mechanics (*35*).

In good agreement with the G&R simulations and experimentally observed spatial variations in material properties, our microscopic observations of vulnerable regions of the aortic wall revealed inhomogeneities in the adventitial:medial ratio between the convex and concave regions of the tortuous samples. In particular, the observed age-related and regional differences in the arrangement of collagen fibers can be associated with the local variations in material stiffness observed in both the pDIC + OCT experiments and simulations. While comparable losses of elastic fiber integrity have been observed in $Fbln5^{-/-}$ arteries from early stages of maturation (*13*), reorientations from an axial to a more diagonal arrangement of collagen fibers in adult $Fbln5^{-/-}$ mice, due to aging and different collagen fiber organization as a function of characteristic regions and age, appear related to the degree of tortuosity and disease progression. In this regard, the experimentally quantified local microstructural variations due to arterial aging may suggest, in line with our quantification of the in vitro tortuosity and finite element G&R simulations, a local (incomplete) restorative process against tortuosity (see fig. S7, third row) that evolves during aging and that needs to be further investigated.

No model, animal or computational, captures completely the human condition. We submit, nonetheless, that the $Fbln5^{-/-}$ aorta is a good in vivo model of tortuosity that develops naturally and arises in the presence of compromised elastic fiber integrity, consistent with many clinical conditions (*4*–*6*, *8*). Although the pDIC + OCT system allowed the first detailed quantification of regional differences in material properties in a tortuous aorta, the method of cannulation and lack of perivascular tethering invariably altered the geometry and wall stress from in vivo. Similarly, the computational model captured many salient features of mechanobiological G&R in arteries, yet it neglected potentially important effects of regional variations in flow-induced wall shear stress and fully 3D perivascular tethering, including branch sites. The in vivo state is thus more complex than that considered here. Nevertheless, the simulations delineated critical differences between uniform and nonuniform geometry, material properties, and external loading and similarly between isotonic and isometric end conditions (Fig. 5). Our simulations also distinguished two remarkably different competing mechanisms by which these vessels may become tortuous, namely, a progressive axial growth–induced tortuous remodeling under constant pressure (Fig. 6) and a transient pressure–induced tortuous distension with preserved mass (fig. S6), with only the former leading to a persistent tortuosity as observed in vivo and the latter only manifesting in previously compromised vessels (see fig. S7, first row). These predictions are consistent with observations that sustained increases in pressure may induce extreme tortuosity of the descending thoracic aorta via vessel wall hypertrophy (*36*), which, nonetheless, manifested only when hypertension was superimposed on an otherwise vulnerable, partially tortuous vessel (fig. S7, second row). We thus submit that this novel experimental-computational approach reliably uncovered heretofore unappreciated mechanics-driven mechanobiological instabilities that contribute to a progressive, persistent tortuosity and can be studied against additional competing hypotheses in the future.

In summary, there have been multiple calls to consider G&R processes in the possible emergence and development of tortuosity (*10*, *11*, *17*, *18*), but the requisite biomechanical data had not been available and an appropriate theoretical and computational framework

capable of describing the nonlinear (including post-buckling) behavior of arteries consisting of multiple constituents had not been used. Both previous limitations were addressed here. Our results suggest that aortic tortuosity need not arise from an instantaneous elastic buckling instability. Rather, ubiquitous mechanosensitive cellular responses to localized microstructural abnormalities can initiate G&R responses to multiple conspiring insults that collectively lead to progressive, persistent tortuosity as the vessel attempts to adapt in the presence of kinematic constraints at branches and sites of strong perivascular tethering; initial axial unloading and elevated blood pressure can exacerbate this mechanobiological structural instability. Our findings are thus consistent with both an in vivo study and suggestion that "longitudinal tissue elaboration must first off-load the axial strain before tortuosity is manifest" (*19*) and increasing clinical intuition that "vascular elongation between 2 fixed points will give rise to tortuosity" (*6*) but bring into focus the probable role of marked microstructural aberrations and local imperfections. This interpretation further focuses attention toward the phenotype of the intramural cells that are responsible for maintaining, remodeling, and repairing the arterial wall locally, which promises to lead to greater insight into the potential of tortuosity as a biomarker rather than simply as a structural anomaly that disturbs blood flow.

MATERIALS AND METHODS

Animals

The Institutional Animal Care and Use Committee of Yale University approved all animal procedures. Fifteen female wild-type ($Fbln5^{+/+}$) and fibulin-5–null ($Fbln5^{-/-}$) mice were euthanized at 20 ± 0.3 (n = 7) or 52 ± 1.8 (n = 8) weeks of age, and the descending thoracic aorta was excised from the first to the fifth pair of intercostal branches and prepared for biomechanical testing. These four primary groups of mice were tested to study the effects of genotype and age on potential aortic tortuosity. Blood pressures were measured 3 to 7 days before euthanasia using a CODA tail-cuff system (Kent Scientific Corporation, Torrington, CT); the mice were euthanized via an intraperitoneal injection of Beuthanasia-D.

Standard biaxial biomechanical testing

Excess perivascular tissue was removed from the excised aortic segments, and intercostal branches were ligated individually using single strands from 7-0 nylon suture. Specimens were then cannulated on and secured to glass cannulas using 6-0 sutures and then placed within a custom computer-controlled testing system for biaxial distension-extension testing, as described previously (*37*). Briefly, following a 15-min acclimation of the aorta within a Hank's buffered salt solution (HBSS) at room temperature (which minimizes contractile tone), mean arterial pressure, and estimated in vivo axial stretch, four preconditioning cycles consisted of pressurization from 10 to 140 mmHg at the fixed axial stretch. Next, each sample was subjected to cyclic pressure–diameter tests at each of three fixed axial lengths (in vivo value and ±5% of this length) and cyclic axial force–length tests at each of four fixed pressures (10, 60, 100, and 140 mmHg), with a maximal allowed axial load of 2 to 2.5 g (~20 to 25 mN).

Data from the last cycle of the unloading curve from all seven protocols were combined and used to determine the best-fit values of the material parameters in a validated four-fiber family constitutive model to describe the overall bulk passive mechanical behavior, as described previously (*24*, *37*). See table S1.

Optical coherence tomography

Following the distension-extension protocols, the samples were re-cannulated on a custom blunt-ended triple-needle assembly (using the same suture locations as in the biaxial test) with the proximal end of the sample secured to a fixed needle and the distal end to a sliding one, thus allowing pressurization and axial stretching (fig. S2). The re-cannulated samples were scanned with a commercially available OCT system (Thorlabs Inc.) to provide through-the-wall thickness information along the entire circumference and axial length, with an in-plane resolution of ~7 μm. Samples were set at a consistent in vitro reference configuration defined by the specimen-specific in vivo value of axial stretch and a common pressure of 80 mmHg. Then, 100 cross-sectional images were acquired along the axial length of the sample (suture-to-suture), yielding an axial spatial resolution of ~60 to 80 μm (depending on sample length). Because of a limited optical penetration depth, samples were scanned from four different rotational views (about the central axes of the vessel) to obtain sufficient information for a 3D reconstruction.

Multiphoton microscopy

Next, the needle assembly supporting the sample was moved to a two-photon microscope (Chameleon Vision II, Coherent) with a titanium-sapphire laser tuned at 840 nm and equipped with a water immersion 20× objective lens [numerical aperture (NA) of 0.95]. The second-harmonic signal arising from collagen structures was detected at the wavelength range of 390 to 425 nm, and autofluorescence of the elastin structures was collected at the range of 500 to 550 nm. 3D images represented a volume of 0.05 mm^3 with an in-plane area of 500 μm × 500 μm. The numerical resolution was 0.48 μm/pixel, and the out-of-plane step was 1 μm/pixel.

By mounting the needle within a custom-built support, distending pressure and axial stretch were controlled while the specimen remained in HBSS at room temperature. Moreover, the needle could be revolved manually about its long axis before a given image acquisition, thus ensuring perpendicularity between the axis of the needle and that of the objective, which was centered over a specific region of interest. Again, the sample was preconditioned, this time via five cycles of pressurization from 10 to 140 mmHg. Next, the distending pressure was fixed sequentially at 40, 80, and 120 mmHg, each at the in vivo value of axial stretch, thus allowing 3D imaging within multiple states and multiple (four) regions, focusing in particular on the two convex and two concave areas of the tortuous samples.

Panoramic digital image correlation

We previously developed a digital image correlation method specifically for quantifying the 3D geometry and full-field multiaxial surface strains on small arteries (*38*). Briefly, following the distension-extension testing as well as the OCT and multiphoton imaging, the samples were stained with Evans blue dye and gently airbrushed with white India ink to form a random characteristic white speckle pattern on a dark blue background (fig. S2), which does not affect the mechanical properties of the arterial wall. The samples (still mounted on the custom blunt-ended triple-needle assembly) were placed coaxially (i.e., aligned vertically) within a 45° angle conical mirror (fig. S2) and again submerged in an HBSS-filled bath at room temperature. This allowed the speckle pattern to be reflected on the inner surface of the conical mirror and captured by a single, vertically positioned digital camera (DALSA Falcon 4M30) from eight symmetric rotational views relative to the central axis of the mirror (fig. S2). Data

were acquired at multiple quasi-statically loaded combinations: 14 different pressures (10 to 140 mmHg in 10-mmHg increments) at three different axial stretches (as in the biaxial test). For computational convenience, the reference configuration was chosen at the in vivo value of axial stretch and a pressure of 80 mmHg.

Last, following all measurements, average values of unloaded wall thickness were measured from transversely cut rings using a dissection microscope, as reported previously (*37*). These values along with the OCT-based data of the reference configuration were used for both the standard biaxial characterization and estimation of the wall thickness for all reconstructed pDIC surfaces, under the common assumptions of a thick wall incompressible body and isochoric motions. See table S1.

OCT and pDIC data analysis

Using custom MATLAB scripts, the many pDIC images were unwrapped and a nodal grid of surface positions was defined across the outer surface of the samples. Serial correlations were performed over all (neighboring) deformed configurations to compute the full-field surface deformations at these nodes and to reconstruct the 3D surface geometry for each deformed configuration. As described previously (*27*), the many OCT images (4 views for each of the 100 cross-sectional views) were co-registered to obtain a 3D OCT reconstruction of each aorta using an iterative multistep registration scheme in 3D Slicer. Once complete, contours of the inner and outer wall were segmented in each cross-sectional image with co-registration between the reconstructed pDIC surface and OCT contours, by single value decomposition, to identify the optimal 3D rigid transformation, mapping thickness values on the pDIC-derived surfaces. Note that the local thickness value, h_{mn}, assigned for each discrete patch and calculated as the distance between the inner and outer wall contours, was not necessarily the precise local thickness of the vessel itself, as the cross-sectional plane may not always align perfectly normal to the vessel surface.

For parameter estimation, a cylindrical coordinate system was defined with $Z \in [O, L]$ and $\Theta \in [-180,180]$ coordinates (where L is the reference length of the sample) and the surface of each configuration was meshed with 40 circumferential (denoted Θ_m, $1 \le m \le 40$) by 25 axial (denoted Z_n, $1 \le n \le 25$) patches (fig. S2), which with the co-registered OCT images allowed the construction of eight-noded 3D hexahedral elements. All reconstructed configurations were rotated such that intercostal branches were positioned at 90° (Fig. 3). Displacement fields were then derived from the surface deformations, thus allowing the calculation of the Green strains for each surface patch at each configuration (*35*). Further details on the pDIC system and analysis can be found elsewhere (*27*, *38*). Note that the upper and lower 10% of the sample (Z_n, $1 \le n \le 3$ and $23 \le n \le 25$) were excluded from the analysis to eliminate edge effects due to cannulation and suture ligation.

Inverse characterization of regional mechanical properties

The pDIC-derived point-wise displacement field was assigned to the 40×25 outer surface nodes as Dirichlet boundary conditions, and distending pressure was prescribed as tractions acting normal to each inner surface node. An incompressible neo-Hookean strain energy function was first used to solve a finite element model in the open-source finite element package FEBio (febio.org), thus yielding Green strains at each Gauss point. Previous experience with murine arteries showed that a microstructurally motivated constrained mixture model describes well the constitutive behavior (*27*). Thus, the passive material behavior was then modeled at each Gauss point k as hyperelastic with a strain energy function, defined per unit mass, of the form

$$W_k = \varphi^e W_k^e + \varphi^\theta W_k^\theta + \varphi^z W_k^z + \varphi^d W_k^d \quad (1)$$

where the elastin-dominated (superscript e) matrix was modeled with a neo-Hookean strain energy function, and the circumferential (θ, muscle and collagen), axial (z, collagen), and diagonal (d, collagen) contributions of the matrix to the mechanical response were modeled with respective Fung-type exponential strain energy functions (*27*). The constituent-specific and (collagen) orientation-specific mass fractions φ^e, φ^θ, φ^z, and φ^d were assigned on the basis of a previous histological report of wall composition in the descending thoracic aorta of *Fbln5*$^{+/+}$ and *Fbln5*$^{-/-}$ mice (overall mass fractions for elastin, ϕ^e, smooth muscle, ϕ^m, and collagen, ϕ^c; table S2) (*24*) while accounting for the respective contribution (β^θ, β^d, and β^z; table S2) of each collagen fiber family, which was determined, in combination with other parameters in table S2, by fits to biaxial data (*28*).

To calculate the wall stress field at each Gauss point k and the local material parameters for the $\Theta_m Z_n$ elements, the principle of virtual power was used to achieve inverse characterization. A cost function J_k involving experimentally measured and theoretically predicted pressures and axial loads (thin wall assumption) was calculated (*27*), and all unknown parameters were updated iteratively until the objective function J_k was minimized (with a stopping criteria of 30 s per node and tolerance of 10^{-6} from one iteration to the next), signifying final parameter identification. Minimization of J_k with respect to the unknown linear parameters was achieved via a non-negative linear least square algorithm and for the remaining nonlinear parameters via a bounded genetic algorithm. Following the inverse characterization, the final set of the identified parameters at each element was used to compute the full-field distributions of various mechanical metrics, in particular, circumferential and axial material stiffness at the sample-specific in vivo axial stretch and systolic pressure of 120 mmHg, as measured with the tail-cuff system, and stored energy at either diastole (80 mmHg) or systole (120 mmHg). For further details on the formulation of the inverse method used here and discussion on its relevance and uncertainty, see Bersi *et al.* (*27*).

Centerlines and tortuosity index

The subroutine vmtkcenterlines, from the open-source Vascular Modeling Toolkit (vmtk.org), was used to compute centerlines for each 3D reconstructed configuration. Briefly, source and target seed points were chosen on the proximal and distal ends of the reconstructed vascular segment, and centerlines were determined as the weighted shortest paths traced between those points. To ensure path centrality, they were bound to run on the Voronoi diagram of the vessel so as to minimize the integral of the radius of maximal inscribed spheres along the path. For further details, see Antiga *et al.* (*39*). Sample-specific centerlines were then used to calculate tortuosity index (TI) as

$$TI = \frac{L_1 - L_2}{L_2} \quad (2)$$

where L_1 is the total length of the aortic centerline and L_2 is its end-to-end distance. Values of TI were quantified at each pressure for the specimen-specific in vivo axial stretch for non-tortuous *Fbln5*$^{+/+}$ and tortuous *Fbln5*$^{-/-}$ samples. Note that the tortuous nature of the latter is characterized by low frequency and high amplitude. It was

for this reason that this particular measure of tortuosity was adopted, yet, for completeness, other methods were computed and yielded similar behavior. Other frequencies and amplitudes exist in other types of tortuous vessels in vivo, but we focused on the descending thoracic aorta alone.

Last, for the regional data analyses, inflection points (defined as relative extreme points) on the centerlines were used to divide the *Fbln5*$^{-/-}$ samples into four different regions along the long axis of the vessel (proximal, $3 < Z < 14$, and distal, $14 \leq Z < 23$) and around its circumference (convex-concave), with approximately $n = 100$ elements per region (Fig. 3).

Multiphoton image analysis

All acquired 3D images were processed with a custom MATLAB ImageJ algorithm. Because of the nearly cylindrical shape of the samples, the structural layers did not reside within circumferential-axial planes. Thus, images were transformed before analysis: 3D images were sliced pixel by pixel in the circumferential-radial plane, and the 2D mid-thickness profile of the wall was used to fit a circle and obtain the centerline coordinates of the latter. The averaged coordinates of the center were used to perform a Cartesian-to-polar transformation of all circumferential-radial slices. Because the radius of the cylinder was more than five times the size of the image in the radial direction, distortions in microstructure due to the transformation were considered negligible. To capture microstructural metrics that reflected the aforementioned biomechanical quantities of interest, the analysis focused on layer-specific thickness and in-plane dispersion of the orientations of the collagen fibers. The layer-specific thickness was obtained by plotting the mean intensity profile for the two constituents (collagen and elastin) along the thickness and then automatically demarcating the adventitial and medial layers via mean intensity values. The automatic decision algorithm was previously tuned by using manual selection inputs from multiple 3D images of murine aortas.

The in-plane dispersion of orientations of the fibers was a measure of the spreading of the collagen fibers around their primary orientations. Considering previous analyses (*40*), collagen fibers show a negligible out-of-plane orientation component. Therefore, the in-plane distribution of orientations was estimated using a 2D structure tensor analysis with OrientationJ implemented for ImageJ. Normalized in-plane distributions of orientation were obtained for all 3D images and showed the existence of a single in-plane primary orientation in the axial direction. The distribution was parameterized using a Von Mises circular probability density function

$$f(\theta \mid \mu, \kappa) = \frac{1}{2\pi I_0(\kappa)} e^{\kappa \cos(\theta - \mu)} \tag{3}$$

depending on angle θ, where $I_0(\kappa)$ is the modified Bessel function of order 0, μ is the principal orientation, and κ is a measure of concentration. The reciprocal $1/\kappa$ was used for the analysis as a measure of dispersion of the collagen fiber orientation.

Statistics

Data were analyzed either by comparing the entire distributions (~800 elements per vessel) of the different mechanical metrics across the four experimental groups (genotype and age) using a two-way analysis of variance (ANOVA), followed by Tukey post hoc test for multiple comparisons, or by comparing different regions (e.g., convex versus concave) within each tortuous sample (*Fbln5*$^{-/-}$) using a one-way ANOVA followed by post hoc Sidak tests. For further interpretation of the regional variations (convex versus concave), Hedge's g statistic was used to measure the effect size following the one-way ANOVA test. Large effect sizes were commonly defined as $g > 0.8$. Significant differences and effect sizes for the regional analysis are summarized in table S3. Because of deviations from normality (Kolmogorov-Smirnov test), differences between TIs among the four study groups were compared with the nonparametric Kruskall-Wallis test followed by Dunn's post hoc test. Differences in the multiphoton microstructural parameters were assessed with a one-way ANOVA followed by post hoc Sidak tests. Correlations between TI and the various mechanical metrics were assessed using the Pearson correlation coefficient, r. For all reported comparisons, a value of $P < 0.05$ was considered significant.

Theoretical G&R framework

The normal thoracic aorta consists of myriad constituents that endow the wall with biomechanical functionality and strength. Most of these constituents can turn over, which enables the aorta to adapt its geometry (e.g., caliber and wall thickness) and composition (e.g., relative contributions of collagen to elastin), and thus biomechanical properties, in response to diverse changes in loading (e.g., blood pressure, flow, or axial stretch) or to actively respond to alterations that occur in diverse disease processes (e.g., progressive endothelial dysfunction)—see Humphrey (*35*) for examples.

Over a period of years, we developed a "constrained mixture model" of arterial growth (changes in mass) and remodeling (changes in microstructure) that accounts for different structurally significant constituents that can have different natural configurations, material properties, and rates of turnover. This model can thus describe and predict the evolving composition, geometry, and nonlinear material properties under many conditions. Briefly, three different constitutive relations (for rates of mass production and removal as well as the passive multiaxial mechanical properties) must be prescribed for each of the structurally significant constituents, which, for convenience, we lump into three groups: elastin-dominated matrix, collagen-dominated matrix, and smooth muscle cells. Because maximum smooth muscle tone is reduced in the aortas of *Fbln5*$^{-/-}$ mice (*41*) and in vivo tone is even less, we neglected contractility here. Thus, the passive biomechanical behavior of the aortic wall is given in terms of the Cauchy stress

$$\boldsymbol{\sigma}(s) = -p(s)\,\mathbf{I} + \frac{2}{J(s)}\mathbf{F}(s)\frac{\partial W_{\mathrm{R}}(s)}{\partial \mathbf{C}(s)}\mathbf{F}^{T}(s) \tag{4}$$

where p is a Lagrange multiplier that enforces isochoric motions during transient loading and $\mathbf{C} = \mathbf{F}^T\mathbf{F}$ is the right Cauchy-Green tensor, computed from the deformation gradient $\mathbf{F}$ from reference to current (in vivo) configurations for the mixture, $W_{\mathrm{R}} = \Sigma\, W_{\mathrm{R}}^{\alpha}$, that is, the total stored energy per unit reference volume W_{R} is the sum of the energies stored in the constituent parts, s is the current G&R time, and $J = \det \mathbf{F}$. For the constituent-specific passive mechanical properties, we let

$$W_R^e(s) = \phi_{\mathrm{R}}^e(s)\,\widehat{W}^e(s) = \phi_{\mathrm{R}}^e(s)\frac{c^e}{2}(\mathrm{tr}(\mathbf{F}^{e\mathrm{T}}(s)\,\mathbf{F}^e(s)) - 3) \tag{5}$$

for the elastin-dominated matrix (e), where $\phi_{\mathrm{R}}^e = J\phi^e$ represents its referential mass fraction within the mixture, $\mathbf{F}^e = \mathbf{F}\mathbf{G}^e$ is the deformation gradient measured from its fixed natural (stress-free)

configuration, with $\mathbf{G}^e$ as a deposition stretch tensor, and c^e is a shear modulus that can be determined from biomechanical testing data. For the energy stored in multiple fiber families, which turn over continuously, we let

$$W_{\mathrm{R}}^{c,m}(s) = \frac{1}{\rho}\int_{-\infty}^{s} m_{\mathrm{R}}^{c,m}(\tau)\, q^{c,m}(s,\tau)\, \widehat{W}^{c,m}\left(\lambda_{\mathrm{n}(\tau)}^{c,m}(s)\right) d\tau \qquad (6)$$

for collagen (c) and passive smooth muscle (m) dominated behaviors, where ρ is the mass density of the tissue, $m_{\mathrm{R}}^{c,m} = \mathrm{J}m^{c,m}$ are referential mass density production rates, τ is the time at which the constituent is produced, and $q^{\alpha}(s,\tau) \in [0,1]$ is an exponential decay function that models removal, where s is the current time of interest. Last, $\lambda_{\mathrm{n}(\tau)}^{c,m}(s)$ is the fiber stretch relative to the associated evolving natural configurations, including the extent of the respective deposition stretches $G^{c,m}$, and

$$\widehat{W}^{c,m}\left(\lambda_{\mathrm{n}(\tau)}^{c,m}(s)\right) = \frac{c_1^{c,m}}{4\,c_2^{c,m}}\left(\exp\left[c_2^{c,m}\left(\left(\lambda_{\mathrm{n}(\tau)}^{c,m}(s)\right)^2 - 1\right)^2\right] - 1\right) \qquad (7)$$

with c_j^i material parameters that can be determined from biaxial mechanical tests on excised arteries. Additional details of the constitutive framework can be found elsewhere (*28*). However, we emphasize that our overall approach enforces mechanical equilibrium quasi-statically ($\mathrm{div}\boldsymbol{\sigma} = \mathbf{0}$) throughout G&R, meaning that progressive processes such as tortuosity are mechanically achievable at every pseudo-time step and they can thereby persist in the absence of loading because load-bearing extracellular matrix turns over in the evolving states.

Model parameters

We used biaxial biomechanical data from a normal descending thoracic aorta from a wild-type ($Fbln5^{+/+}$) mouse to parameterize the baseline biomechanical model, with additional parameters describing the time course of a mechano-adaptive G&R response extracted from Latorre and Humphrey (*42*). Similarly, a set of passive mechanical parameters was determined from biaxial biomechanical data from a representative descending thoracic aorta from a fibulin-5–null ($Fbln5^{-/-}$) mouse. All parameters are listed in table S2. Note that the potentially compromised biomechanical response of the fibulin-5–null mouse does not represent a response that evolved from a normal wild-type mouse because these mice have a germline mutation and thus an independent development and maturation processes. Consequently, the fibulin-5 null–related parameters in table S2, which reveal the main difference in bulk passive mechanical properties between these two genotypes, provide qualitative insight to guide our computational modeling of wild-type aortas that may develop tortuosity due to losses in elastic fiber integrity.

Recall, therefore, that in addition to the general risk factor of aging, compromised elastic fiber integrity (see, e.g., the reduced material parameter c^e and in-plane in vivo pre-stretches G_θ^e and G_z^e for fibulin-5–null mice in table S2) appears to be a major contributor to axial growth–induced tortuosity (*4*, *6*, *7*, *14*, *23*, *24*). To test numerically the potential of compromised elastin to induce axial growth and develop, as a result, tortuous vessels consistent with appropriate initial perturbations and boundary conditions, we gradually prescribed a loss of elastic fiber integrity (described by a maximal ~20% reduction in the value of the elastin-associated material parameter c^e; see table S2) either in isolation or in combination with other potential contributors consistent with differences observed in table S2. Preliminary simulations revealed that the computed axial growth response was notably more pronounced when the prescribed loss of elastic fiber integrity was combined with a deposition of diagonal collagen increasingly oriented toward the circumferential direction (described by a ~30% increase in the value of the collagen-associated material parameter α_0; see table S2). A simultaneous variation of other parameters (e.g., those in the Fung-type exponentials for smooth muscle and collagen fibers) either contributed to the axial growth response to a lesser extent [see Dobrin *et al.* (*14*)] or required complex nonlinear relations among their coupled evolutions to yield realistic (bounded) G&R responses. Hence, as a first illustrative attempt to study axial growth with minimal simultaneous changes in parameters from wild-type to elastic fiber compromised (determined from respective sets of biaxial biomechanical data), we prescribed the desired loss of elastic fiber integrity either in isolation or in combination with the aforementioned increased orientation for diagonal collagen families, with all remaining parameters in our model fixed to baseline (wild-type) values.

Although it has been suggested that elastic buckling may be an initiator of arterial tortuosity (*10*, *11*), it is not yet clear that the geometrical nonuniformities that arise from this instantaneous buckling (a bifurcation response that takes place over a short time scale) can result in persistent tortuosity [a gradual remodeling response that takes place over much longer time scales; (*43*, *44*)]. That is, because a transiently buckled (i.e., bifurcated) vessel adopts a curved geometry (i.e., secondary solution) that breaks overall axisymmetry, it is possible that, rather than being an initiator of permanent tortuosity, this elastic buckling simply represents an initial (geometrical) perturbation that enables an axially constrained and prestressed vessel to develop a growth-induced tortuosity initiated by aging or particular genetic defects (*6*). Other structural (geometrical or material) nonuniformities initially present in the aorta may equally enable a subsequent tortuous enlargement, as we describe next.

Thus, for purposes of illustration, consider an initially perfectly straight cylindrical segment of the thoracic aorta of uniform in vivo wall thickness ($h_o = 0.34$ μm) and luminal radius ($a_o = 568$ μm) into which the following one-wave–like asymmetric (i.e., axially and circumferentially nonuniform, reflecting that observed in a $Fbln5^{-/-}$ sample) material insult is placed

$$\vartheta(r_o,\theta_o,z_o) = \vartheta_{\mathrm{WT}} + \frac{1}{2}(\vartheta - \vartheta_{\mathrm{WT}}) + \frac{1}{2}(\vartheta - \vartheta_{\mathrm{WT}})\frac{1}{2}\left(1 - \cos\frac{2\pi z_o}{l_o}\right)\exp\left(-\left|\frac{\theta_o - \hat{\theta}}{2\pi}\right|^2\right) \qquad (8)$$

where $r_o \in [a_o,\, a_o + h_o]$, $\theta_o \in [0,2\pi]$, and $z_o \in [0,2l_o]$ are the radial, circumferential, and axial coordinates in the reference (homeostatic) configuration, respectively; ϑ_{WT} is the baseline [wild-type (WT)] value of the associated material parameter (c^e or α_0); and ϑ is the stimulation driver for the quasi-static G&R response with $\hat{\theta} = \hat{\theta}_1 = \pi$ for $z_o \in [0,\, l_o]$ and $\hat{\theta} = \hat{\theta}_2 = \pi - \hat{\theta}_1 = 0$ for $z_o \in [l_o, 2l_o]$. We start our simulations from $\vartheta = \vartheta_{\mathrm{WT}}$, for which $\vartheta(r_o,\, \theta_o,\, z_o) = \vartheta_{\mathrm{WT}}$ is uniform, and then vary ϑ up to $\vartheta = \vartheta_{\mathrm{KO}}$, for which $\vartheta\left(r_o, \theta_o^{\mathrm{cr}}, z_o^{\mathrm{cr}}\right) = \vartheta\left(r_o, \theta_o^{\mathrm{tr}}, z_o^{\mathrm{tr}}\right) = \vartheta_{\mathrm{KO}}$ at the crest $\left(\theta_o^{\mathrm{cr}} = \pi, z_o^{\mathrm{cr}} = l_o/2\right)$ and trough $\left(\theta_o^{\mathrm{tr}} = 0,\ z_o^{\mathrm{tr}} = 3\,l_o/2\right)$ of the computational aorta. That is, rather than starting our G&R simulations from a geometrical nonuniformity with uniform material properties (e.g., a buckled artery), we prescribe a material nonuniformity on a uniform straight artery to enable differential (regional) axial growth responses that can potentially induce

a mechanobiological structural instability and subsequent tortuosity. Furthermore, note that we can first prescribe a nonuniform perturbation in parameters on the normal aorta via the third term on the right-hand side in Eq. 8 and, subsequently, prescribe an incremental uniform insult via the second term (see Figs. 5, first row, and 6). Alternatively, a uniform change in these elastin-collagen parameters $\vartheta \in [\vartheta_{WT}, \vartheta_{KO}]$ prescribed on an initially undulated artery (as a result of nonuniform tethering or geometric imperfections) can, similarly, give rise to axial growth–induced elongation and tortuosity (Fig. 5, second and third rows).

Here, we use a fast, efficient 3D implementation (*28*) that is fully nonlinear (materially and geometrically, properly accounting for finite strains and rotations) and based on the underlying assumption that each G&R state is mechanobiologically equilibrated, which holds for cases wherein the characteristic time scale of the remodeling process is shorter than the stimulation time scale, that is, fully quasi-static G&R. This rate-independent formulation eliminates dependence on G&R time s and allows equilibrium to be enforced in vivo in homeostatic grown and remodeled states for given external loads and boundary conditions. In particular, mechanobiological equilibrium leads to $W_{Rh}^{c,m} = \phi_{Rh}^{c,m}\widehat{W}^{c,m}(G_h^{c,m})$ in Eq. 6, which, in combination with an equilibrated energy for elastin in Eq. 5, leads to a rule-of-mixtures relation for the total energy $W_{Rh} = \Sigma\phi_{Rh}^{\alpha}\widehat{W}^{\alpha}$ with evolved constituent mass fractions and deformations. The Cauchy stress in Eq. 4 also adopts a rule-of-mixtures expression in terms of evolved constituent-specific passive stresses

$$\boldsymbol{\sigma}_h = \sum_{\alpha}^{e,c,m} \phi_h^{\alpha}\widehat{\boldsymbol{\sigma}}_h^{\alpha} - p_h\mathbf{I} \tag{9}$$

with the Lagrange multiplier p_h consistently determined from a mechanobiological equilibrium constraint (that enforces a balanced production and removal of constituents) during the quasi-static G&R evolution. A consistent linearization of the formulation enables implementation within a finite element framework, where simultaneous solution of mechanical and mechanobiological equilibrium can be ensured efficiently at successive load steps that capture evolving geometries, compositions, and properties of interest for complex boundary value problems, including post-buckling–like responses that give rise to persistent tortuosity.

Last, our nonlinear computational model of the aortic wall allows us to compute many important biomechanical metrics, including biaxial (circumferential and axial) wall stretch, stress, and material stiffness as well as elastic energy storage. The finite element model for the initially straight cylindrical segment of the thoracic aorta comprised $N_r N_\theta N_z = 1 \times 20 \times 40 = 800$ displacement-based 3D quadratic elements with full $3 \times 3 \times 3$ Gauss integration and was computed quasi-statically in a modified open-source code FEBio; see additional constitutive, algorithmic, and computational details in the study of Latorre and Humphrey (*28*).

SUPPLEMENTARY MATERIALS

Supplementary material for this article is available at http://advances.sciencemag.org/cgi/content/full/6/49/eabd3574/DC1

View/request a protocol for this paper from *Bio-protocol*.

REFERENCES AND NOTES

1. J. Humphrey, Vascular adaptation and mechanical homeostasis at tissue, cellular, and sub-cellular levels. *Cell Biochem. Biophys.* **50**, 53–78 (2008).
2. P. J. Coucke, A. Willaert, M. W. Wessels, B. Callewaert, N. Zoppi, J. De Backer, J. E. Fox, G. M. Mancini, M. Kambouris, R. Gardella, F. Facchetti, P. J. Willems, R. Forsyth, H. C. Dietz, S. Barlati, M. Colombi, B. Loeys, A. De Paepe, Mutations in the facilitative glucose transporter GLUT10 alter angiogenesis and cause arterial tortuosity syndrome. *Nat. Genet.* **38**, 452–457 (2006).
3. S. A. Morris, D. B. Orbach, T. Geva, M. N. Singh, K. Gauvreau, R. V. Lacro, Increased vertebral artery tortuosity index is associated with adverse outcomes in children and young adults with connective tissue disorders. *Circulation* **124**, 388–396 (2011).
4. R. Franken, A. El Morabit, V. de Waard, J. Timmermans, A. J. Scholte, M. P. van den Berg, H. Marquering, N. R. Planken, A. H. Zwinderman, B. J. Mulder, M. Groenink, Increased aortic tortuosity indicates a more severe aortic phenotype in adults with Marfan syndrome. *Int. J. Cardiol.* **194**, 7–12 (2015).
5. A. Beyens, J. Albuisson, A. Boel, M. Al-Essa, W. Al-Manea, D. Bonnet, O. Bostan, O. Boute, T. Busa, N. Canham, E. Cil, P. J. Coucke, M. A. Cousin, M. Dasouki, J. De Backer, A. De Paepe, S. De Schepper, D. De Silva, K. Devriendt, I. De Wandele, D. R. Deyle, H. Dietz, S. Dupuis-Girod, E. Fontenot, B. Fischer-Zirnsak, A. Gezdirici, J. Ghoumid, F. Giuliano, N. B. Diéz, M. Z. Haider, J. S. Hardin, X. Jeunemaitre, E. W. Klee, U. Kornak, M. F. Landecho, A. Legrand, B. Loeys, S. Lyonnet, H. Michael, P. Moceri, S. Mohammed, L. Muiño-Mosquera, S. Nampoothiri, K. Pichler, K. Prescott, A. Rajeb, M. Ramos-Arroyo, M. Rossi, M. Salih, M. Z. Seidahmed, E. Schaefer, E. Steichen-Gersdorf, S. Temel, F. Uysal, M. Vanhomwegen, L. Van Laer, L. Van Maldergem, D. Warner, A. Willaert, T. R. Collins, A. Taylor, E. C. Davis, Y. Zarate, B. Callewaert, Arterial tortuosity syndrome: 40 new families and literature review. *Genet. Med.* **20**, 1236–1245 (2018).
6. S. Ciurică, M. Lopez-Sublet, B. L. Loeys, I. Radhouani, N. Natarajan, M. Vikkula, A. H. Maas, D. Adlam, A. Persu, Arterial tortuosity: Novel implications for an old phenotype. *Hypertension* **73**, 951–960 (2019).
7. H.-C. Han, Twisted blood vessels: Symptoms, etiology and biomechanical mechanisms. *J. Vasc. Res.* **49**, 185–197 (2012).
8. S. A. Morris, Arterial tortuosity in genetic arteriopathies. *Curr. Opin. Cardiol.* **30**, 587–593 (2015).
9. R. M. Vandiver, Buckling instability in arteries. *J. Theor. Biol.* **371**, 1–8 (2015).
10. H.-C. Han, J. K. Chesnutt, J. R. Garcia, Q. Liu, Q. Wen, Artery buckling: New phenotypes, models, and applications. *Ann. Biomed. Eng.* **41**, 1399–1410 (2013).
11. C. M. Luetkemeyer, R. H. James, S. T. Devarakonda, V. P. Le, Q. Liu, H.-C. Han, J. E. Wagenseil, Critical buckling pressure in mouse carotid arteries with altered elastic fibers. *J. Mech. Behav. Biomed. Mater.* **46**, 69–82 (2015).
12. J. E. Wagenseil, R. P. Mecham, Vascular extracellular matrix and arterial mechanics. *Physiol. Rev.* **89**, 957–989 (2009).
13. W. Wan, R. L. Gleason Jr., Dysfunction in elastic fiber formation in fibulin-5 null mice abrogates the evolution in mechanical response of carotid arteries during maturation. *Am. J. Phys. Heart Circ. Phys.* **304**, H674–H686 (2013).
14. P. B. Dobrin, T. Schwarcz, W. Baker, Mechanisms of arterial and aneurysmal tortuosity. *Surgery* **104**, 568–571 (1988).
15. A. Y. Lee, B. Han, S. D. Lamm, C. A. Fierro, H.-C. Han, Effects of elastin degradation and surrounding matrix support on artery stability. *Am. J. Phys. Heart Circ. Phys.* **302**, H873–H884 (2012).
16. D. M. Hayman, J. Zhang, Q. Liu, Y. Xiao, H.-C. Han, Smooth muscle cell contraction increases the critical buckling pressure of arteries. *J. Biomech.* **46**, 841–844 (2013).
17. A. Goriely, R. Vandiver, On the mechanical stability of growing arteries. *IMA J. Appl. Math.* **75**, 549–570 (2010).
18. Z. S. Jackson, A. I. Gotlieb, B. L. Langille, Wall tissue remodeling regulates longitudinal tension in arteries. *Circ. Res.* **90**, 918–925 (2002).
19. Z. S. Jackson, D. Dajnowiec, A. I. Gotlieb, B. L. Langille, Partial off-loading of longitudinal tension induces arterial tortuosity. *Arterioscler. Thromb. Vasc. Biol.* **25**, 957–962 (2005).
20. R. L. Gleason, E. Wilson, J. D. Humphrey, Biaxial biomechanical adaptations of mouse carotid arteries cultured at altered axial extension. *J. Biomech.* **40**, 766–776 (2007).
21. J. Humphrey, J. Eberth, W. Dye, R. Gleason, Fundamental role of axial stress in compensatory adaptations by arteries. *J. Biomech.* **42**, 1–8 (2009).
22. F. Cuomo, S. Roccabianca, D. Dillon-Murphy, N. Xiao, J. D. Humphrey, C. A. Figueroa, Effects of age-associated regional changes in aortic stiffness on human hemodynamics revealed by computational modeling. *PLOS ONE* **12**, e0173177 (2017).
23. A. M. Tawfik, D. M. Sobh, B. Gadelhak, H. M. Sobh, N. M. Batouty, The effect of age and gender on tortuosity of the descending thoracic aorta. *Eur. J. Radiol.* **110**, 54–59 (2019).
24. J. Ferruzzi, M. Bersi, S. Uman, H. Yanagisawa, J. Humphrey, Decreased elastic energy storage, not increased material stiffness, characterizes central artery dysfunction in fibulin-5 deficiency independent of sex. *J. Biomech. Eng.* **137**, 0310071–03100714 (2015).
25. F. Cuomo, J. Ferruzzi, P. Agarwal, C. Li, Z. W. Zhuang, J. D. Humphrey, C. A. Figueroa, Sex-dependent differences in central artery haemodynamics in normal and fibulin-5 deficient mice: Implications for ageing. *Proc. R. Soc. A* **475**, 20180076 (2019).

26. B. Spronck, J. Ferruzzi, C. Bellini, A. W. Caulk, S.-I. Murtada, J. D. Humphrey, Aortic remodeling is modest and sex-independent in mice when hypertension is superimposed on aging. *J. Hypertens.* **38**, 1312–1321 (2020).
27. M. R. Bersi, C. Bellini, J. D. Humphrey, S. Avril, Local variations in material and structural properties characterize murine thoracic aortic aneurysm mechanics. *Biomech. Model. Mechanobiol.* **18**, 203–218 (2019).
28. M. Latorre, J. D. Humphrey, Fast, rate-independent, finite element implementation of a 3D constrained mixture model of soft tissue growth and remodeling. *Comput. Meth. Appl. Mech. Eng.* **368**, 113156 (2020).
29. P. Badel, C. P.-Y. Rohan, S. Avril, Finite Element simulation of buckling-induced vein tortuosity and influence of the wall constitutive properties. *J. Mech. Behav. Biomed. Mater.* **26**, 119–126 (2013).
30. Q. Liu, Q. Wen, M. Mottahedi, H.-C. Han, Artery buckling analysis using a four-fiber wall model. *J. Biomech.* **47**, 2790–2796 (2014).
31. P. Bayly, R. Okamoto, G. Xu, Y. Shi, L. Taber, A cortical folding model incorporating stress-dependent growth explains gyral wavelengths and stress patterns in the developing brain. *Phys. Biol.* **10**, 016005 (2013).
32. S. Budday, P. Steinmann, E. Kuhl, The role of mechanics during brain development. *J. Mech. Phys. Solids* **72**, 75–92 (2014).
33. Y. Jiao, G. Li, A. Korneva, A. W. Caulk, L. Qin, M. R. Bersi, Q. Li, W. Li, R. P. Mecham, J. D. Humphrey, G. Tellides, Deficient circumferential growth is the primary determinant of aortic obstruction attributable to partial elastin deficiency. *Arterioscler. Thromb. Vasc. Biol.* **37**, 930–941 (2017).
34. D. Dajnowiec, P. J. Sabatini, T. C. Van Rossum, J. T. Lam, M. Zhang, A. Kapus, B. L. Langille, Force-induced polarized mitosis of endothelial and smooth muscle cells in arterial remodeling. *Hypertension* **50**, 255–260 (2007).
35. J. Humphrey, *Cardiovascular Solid Mechanics: Cells, Tissues and Organs* (Springer-Verlag, 2002).
36. L. Del Corso, D. Moruzzo, B. Conte, M. Agelli, A. M. Romanelli, F. Pastine, M. Protti, F. Pentimone, G. Baggiani, Tortuosity, kinking, and coiling of the carotid artery: Expression of atherosclerosis or aging? *Angiology* **49**, 361–371 (2016).
37. J. Ferruzzi, M. Bersi, J. Humphrey, Biomechanical phenotyping of central arteries in health and disease: Advantages of and methods for murine models. *Ann. Biomed. Eng.* **41**, 1311–1330 (2013).
38. K. Genovese, Y. Lee, A. Lee, J. Humphrey, An improved panoramic digital image correlation method for vascular strain analysis and material characterization. *J. Mech. Behav. Biomed. Mater.* **27**, 132–142 (2013).
39. L. Antiga, B. Ene-Iordache, A. Remuzzi, Centerline computation and geometric analysis of branching tubular surfaces with application to blood vessel modeling, in *11th International Conference in Central Europe on Computer Graphics, Visualization and Computer Vision 2003* (UNION Agency, 2003).
40. C. Cavinato, C. Helfenstein-Didier, T. Olivier, S. R. Du Roscoat, N. Laroche, P. Badel, Biaxial loading of arterial tissues with 3D in situ observations of adventitia fibrous microstructure: A method coupling multi-photon confocal microscopy and bulge inflation test. *J. Mech. Behav. Biomed. Mater.* **74**, 488–498 (2017).
41. S.-I. Murtada, J. Ferruzzi, H. Yanagisawa, J. Humphrey, Reduced biaxial contractility in the descending thoracic aorta of fibulin-5 deficient mice. *J. Biomech. Eng.* **138**, 051008 (2016).
42. M. Latorre, J. D. Humphrey, Modeling mechano-driven and immuno-mediated aortic maladaptation in hypertension. *Biomech. Model. Mechanobiol.* **17**, 1497–1511 (2018).
43. Ö. Smedby, L. Bergstrand, Tortuosity and atherosclerosis in the femoral artery: What is cause and what is effect? *Ann. Biomed. Eng.* **24**, 474–480 (1996).
44. N. B. Wood, S. Z. Zhao, A. Zambanini, M. Jackson, W. Gedroyc, S. A. Thom, A. D. Hughes, X. Y. Xu, Curvature and tortuosity of the superficial femoral artery: A possible risk factor for peripheral arterial disease. *J. Appl. Physiol.* **101**, 1412–1418 (2006).

Acknowledgments: We thank the staff of the microscopy core at Yale for expert assistance. **Funding:** This work was supported by grants from the U.S. NIH (R01 HL105297, P01 HL134605, and U01 HL142518). **Author contributions:** D.W. and J.D.H. conceived the project. D.W., C.C., and A.B.R. collected the data. D.W., C.C., A.G., and S.A. analyzed the data. M.L., D.W., and J.D.H. conceived the computational study. M.L. performed the computational simulations. D.W., C.C., M.L., and J.D.H. interpreted the results. D.W., M.L., and J.D.H. wrote the manuscript. All authors revised and approved the final manuscript. **Competing interests:** The authors declare that they have no competing interests. **Data and materials availability:** All data needed to evaluate the conclusions in the paper are present in the paper and/or the Supplementary Materials. Additional data related to this paper may be requested from the authors.

Submitted 16 June 2020
Accepted 22 October 2020
Published 4 December 2020
10.1126/sciadv.abd3574

Citation: D. Weiss, C. Cavinato, A. Gray, A. B. Ramachandra, S. Avril, J. D. Humphrey, M. Latorre, Mechanics-driven mechanobiological mechanisms of arterial tortuosity. *Sci. Adv.* **6**, eabd3574 (2020).

Mechanics-driven mechanobiological mechanisms of arterial tortuosity

Dar Weiss, Cristina Cavinato, Authia Gray, Abhay B. Ramachandra, Stephane Avril, Jay D. Humphrey and Marcos Latorre

Sci Adv **6** (49), eabd3574.
DOI: 10.1126/sciadv.abd3574